Journal of Sound and Vibration 604 (2025) 118978

Contents lists available at ScienceDirect

Journal of Sound and Vibration

journal homepage: www.elsevier.com/locate/jsvi

Installation effects on airfoil self-noise estimated by direct numerical simulations

Ziyang Zhou [b,*], Stéphane Moreau [b], Marlène Sanjosé [a]

[a] École de Technologie Supérieure, Mechanical Engineering, 1100 rue Notre Dame Ouest, Montréal, H3C 1K3, Québec, Canada
[b] Université de Sherbrooke, Mechanical Engineering, 2500 boulevard de l'Université, Sherbrooke, J1K 1T1, Québec, Canada

ARTICLE INFO

Keywords:
Aeroacoustics
Aerofoil noise
Direct numerical simulations

ABSTRACT

Several Direct Numerical Simulations (DNS) have been achieved using the Lattice-Boltzmann Method (LBM) on a Controlled-Diffusion (CD) airfoil at $Re_c = 1.5 \times 10^5$ and $\alpha = 8°$ to evaluate installation effects on airfoil self-noise. 2D DNS provides unrealistic airfoil noise sources and a significant overprediction of the far-field noise with possibly a change in the ranking of the noise sources. Conversely, all 3D simulations of the airfoil immersed in the wind tunnel jet show excellent agreement with the flow around the airfoil and the far-field noise. Two new 3D DNS with some shear-layer refinement and possibly an additional zigzag trip to trigger turbulence have better resolved the jet development. Even though all 3D DNS identify two main noise sources, the laminar separation bubble (LSB) at the leading edge and the turbulent eddies at the trailing edge, their intensity varies because of a strong coupling between the jet and the airfoil that yields different LSB sizes, increased inlet turbulent intensity, oscillations of the angle-of-attack, and variations in the noise sources. The state of the jet shear layer at the nozzle exit of a given open-jet anechoic wind tunnel is seen to influence the flow field around the airfoil and its noise radiation, with potentially a larger jet contribution.

1. Introduction

Low speed fans are commonly seen in various applications (e.g. automotive cooling fans [1,2], wind turbines [3], hairdryers [4]), and noise reduction for these rotating machines is becoming a key element. Furthermore, for high-speed turbomachines, with the current trend toward Ultra High Bypass Ratio engines [5], fan noise is expected to form the performance ceiling for noise reduction efforts. Given the projected increase in the significance of fan noise, it is of fundamental interest to study the noise generating mechanisms of modern CD airfoils which are commonly used in the design of both low [6] and high speed fans [7]. Of the various geometric angles of attack studied previously on the CD airfoil with a chord length $c = 0.1356$ m, shown in Fig. 1 equipped with 21 flush-mounted Remote Microphone Probes (RMP), the 8° at a Reynolds number based on the chord $Re_c = 1.5 \times 10^5$ is one of the most widely studied numerically [8–13] and experimentally [14–17], as it corresponds to optimal design conditions [18].

Several experimental studies have been conducted to characterize CD airfoils in open-jet wind tunnels [14–17], but none have focused on the simultaneous measurement of the flow field around the airfoil and the jet shear layer so far. The effect of the wind tunnel installation used in CD airfoil studies has also been extensively documented in these studies. Initial work by Moreau et al. [19] using Reynolds-averaged Navier–Stokes RANS simulations revealed that including the wind tunnel was crucial to achieve good agreement in mean wall-pressure coefficient between experimental and simulation results and that the definition of an effective

* Corresponding author.
E-mail address: zhou.ziyang@usherbrooke.ca (Z. Zhou).

https://doi.org/10.1016/j.jsv.2025.118978
Received 7 March 2024; Received in revised form 21 January 2025; Accepted 22 January 2025
Available online 30 January 2025

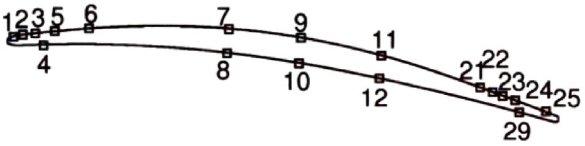

Fig. 1. CD airfoil geometry and RMP locations [25].

Table 1
Summary of simulation configurations considered.

Configuration	Voxels ($\times 10^6$)	U_{ref} (m/s)	Lip BC	Inlet BC	Trip	Shear layer refinement
2D DNS free-field	21	16.3	–	Uniform	–	–
2D DNS Lips	21	16.8	Slip	Profile	No	No
3D DNS	640	16.6	Slip	Profile	No	No
3D DNS-SLR	740	16.6	Slip	Profile	No	Yes
3D DNS-SLRT	1050	16.7	No slip	Uniform	Yes	Yes

angle-of-attack to recover the free-field pressure distribution was not possible for this airfoil. Similar conclusions were reached by Sheikh-AlShabab et al. [20] in their open jet experimental setup. Further studies on the effect of the open jet wind tunnel have also been performed on other airfoils. For example, Moreau et al. [21] conducted aero-acoustic measurements on a NACA0012 airfoil and examined the effect that the width of the jet had on airfoil loading and self noise. A larger jet width resulted in a transition to deep stall at a lower angle of attack and the appearance of two low-frequency peaks associated with stall noise. This shows the close relation between the jet confinement provided by the open jet wind tunnel and the loading experienced by the airfoil under study. In addition to a change in airfoil loading, the shear layer can also cause a change in the angle and amplitude of propagated sound to the far field [22]. Spectral broadening may also occur in which tonal noise is distributed to adjacent frequencies [23,24] due to the influence of the turbulent shear layer.

Most numerical studies of the installed CD airfoil generally only account for the time-averaged effect that the open jet wind tunnel has on the CD airfoil flow field and noise generation (see the review in [18]). The early incompressible LES by Wang et al. [8], Christophe et al. [26] and Winkler et al. [27] have made use of a computational domain embedded in the potential core of the jet using non uniform inflow boundary conditions. Recent DNS done by Wu et al. [9] and Arroyo et al. [28] on the CD airfoil at $\alpha = 8°$ have followed suit. This setup was able to account for the mean deflection of the jet and this was shown by the good agreement of mean pressure coefficient with experimental results. On the other hand, the LBM simulations in [11–13] did include the effects of the shear layer from the wind tunnel by including the lips of the open nozzle in the simulation and imposing a measured inlet profile as boundary condition. Yet, the effect of grid resolution on the shear layer was not studied. As the grid is refined, more time-dependent flow structures are expected to form due to instability in the mixing layer and this is expected to have an effect on airfoil loading and jet noise contribution.

Based on this review, the present investigation aims at achieving the following goals. A first one is to assess installation effects with 2D DNS free-field and installed 2D and 3D DNS, to demonstrate the difference between 2D and 3D results, and to quantify its aero-acoustic impact for the first time. This is all the more important as most DNS on airfoil noise are still 2D because of their large computational cost [29–31]. A second one is to demonstrate the effect of changes in the physical nature of the mixing layer downstream of the wind tunnel lips on airfoil flow regime and on far-field acoustics. The changes to the mixing layer are triggered using grid refinement and a turbulent trip at the appropriate locations. The latter contribution is expected to shed new light on installation effects in airfoil noise experiments, and particularly the coupling that exists between the jet and the airfoil both in terms of flow field and sound. This in turn should guide proper set-ups for both future experiments and simulations on airfoil noise. To achieve these objectives, 5 DNS summarized in Table 1 have been achieved. Their results will be compared with several experiments in different open-jet wind tunnels [15,17,25] and the results of the reference DNS setup by Sanjosé et al. [11].

In the following, Section 2 will give the details of the numerical setup used for this investigation. Section 3 will give the aerodynamic results along with a novel study of the correlation between flow variables in the shear layer and close to the airfoil. The farfield acoustics will be examined in Section 4 and conclusions will be drawn in Section 5.

2. Numerical setup

2.1. Computational domain and methodology

To mimic actual installation effects, the computational domain in all simulations listed in Table 1 but the free-field case corresponds to several open-jet experimental set-ups [11–13]. As shown in Fig. 2(a), it includes the nozzle geometry similar to that used in Université de Sherbrooke (UdeS) and Ecole Centrale de Lyon (ECL) having the same jet width and similar flanges, the CD airfoil placed in the jet potential core, and a significant portion of the anechoic chamber (a box of 4 m^2). For all 3D DNS, a span of 0.12 c is considered, which is based on the experimental spanwise wall-pressure coherence length at the trailing edge [15], as in previous high-fidelity simulations [8,9,12,28]. In the free-field case, the nozzle is simply removed.

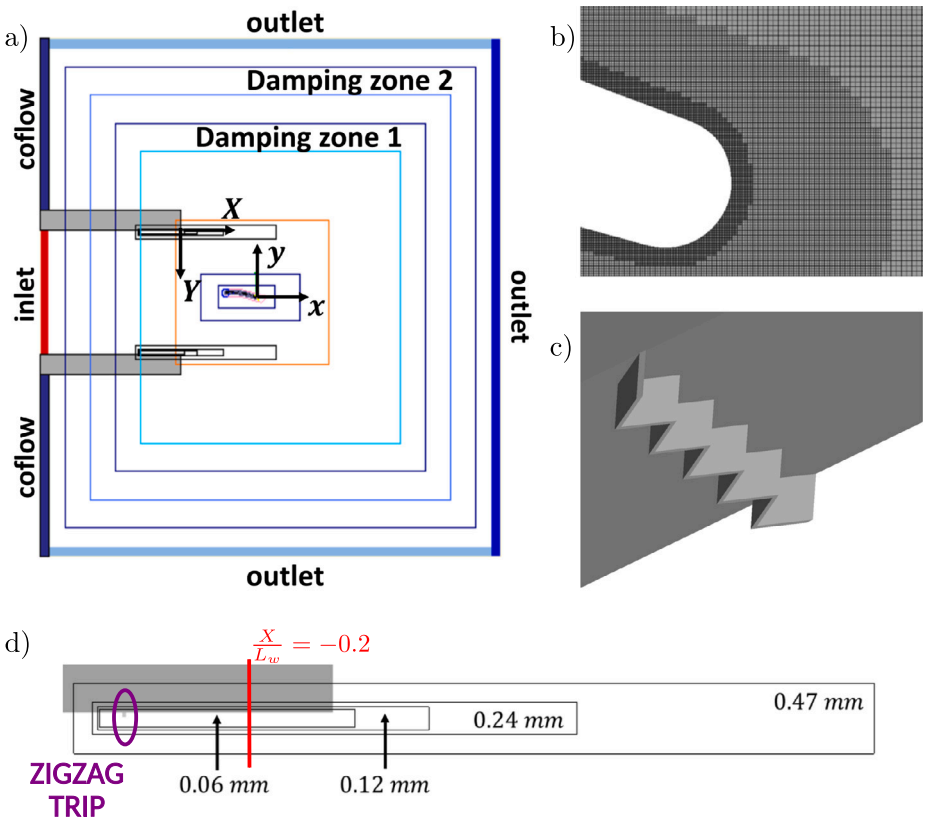

Fig. 2. Numerical configuration: (a) computational domain and coordinate definitions, (b) grid zoom at trailing-edge, (c) zigzag trip, (d) details of voxel refinement for the nozzle boundary layer and jet shear layer. (For interpretation of the references to color in this figure legend, the reader is referred to the web version of this article.)

All present DNS of the CD airfoil at $\alpha = 8°$ and a Reynolds number based on the chord at a Reynolds number based on the chord $Re_c = 1.5 \times 10^5$ have been run with LBM using PowerFLOW 6.2021.R6 [32,33]. This approach has been selected as it is computationally efficient for low speed conditions and handles complex airfoil geometry, and a large domain for acoustic propagation [34–36].

2.2. Meshes

The computational domain is then filled with an octree grid of cubic cells called voxels with a 1:2 grid refinement [37]. In order to resolve smaller flow structures, voxel regions are defined in which the voxel size Δx is specified. Ten voxel regions, shown by the colored lines in Fig. 2(a), are used in the computational domain [11]. The voxel regions are used to impose the required dimensionless wall distance, Δy^+, on the surface of the airfoil and to transition to larger cell sizes in areas further away. The minimum voxel size used on the airfoil surface has a dimension of 0.0148 mm in order to ensure a Δy^+ below 1 over a majority of the airfoil surface as verified in Fig. 3. Consequently, the dimensionless distances in the streamwise, Δx^+, and spanwise, Δz^+, directions are also below 1 ensuring a DNS resolution close to the airfoil. Note also that although the experimental Mach number is 0.05, the Mach number has been increased in the simulation to 0.2. This adjustment is necessary to achieve DNS resolution in the three voxel regions closest to the airfoil. To accommodate this Mach number increase, the lattice velocity must be raised, and consequently, lattice viscosity is also increased to maintain a constant Reynolds number. Due to a stability threshold on the relaxation time, the viscosity in voxel regions beyond the three finest ones is higher than the specified kinematic viscosity of 1.44×10^{-5} m^2/s. The three finest voxel regions shown in Fig. 2(b) cover the size of the boundary layer as measured in [25].

Compared to the 3D DNS setup [11,13], new additional voxel refinement regions are implemented in the shear layer region downstream of the wind tunnel nozzle lip in the 3D DNS-SLR case, as shown in Fig. 2(a, d). Moreover, in the 3D DNS-SLRT case, zigzag trips of height $h = 3.36$ mm are added to trigger transition to turbulence upstream of the lower and upper lips. These trips are placed 50 h upstream of each lip as can be seen in Fig. 2(c). Further grid refinement helps capture the development of the turbulent boundary layer downstream of the zigzag trip. A minimum voxel size of 0.0592 mm is used. This ensures a Δy^+ of 2 at the edge of the lip. As seen in Fig. 4, in the 3D DNS-SLRT case, the boundary layer velocity profile upstream of the nozzle exit at $X/L_w = -0.2$, where L_w is the jet half width agrees well with the log law [38]. This demonstrates that in the 3D DNS-SLRT a fully turbulent state

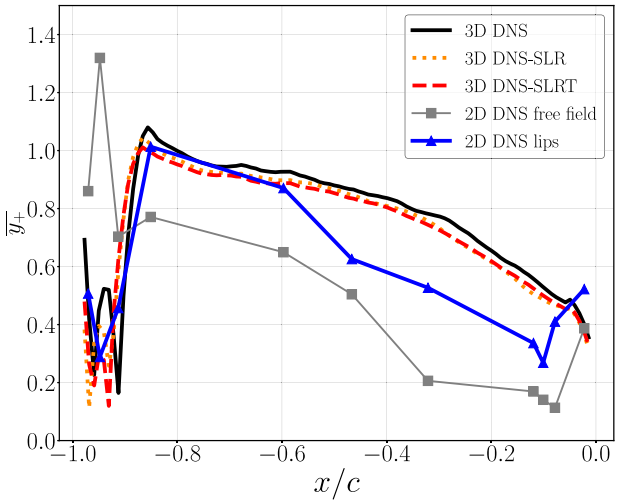

Fig. 3. Plot of y^+ on the airfoil suction side.

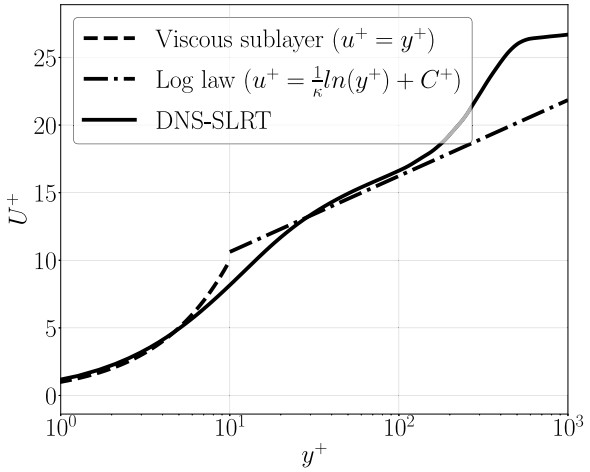

Fig. 4. Boundary layer velocity profile upstream of the nozzle exit ($X/L_w = -0.2$).

is achieved at end of the nozzle lips. Furthermore, this voxel region setup ensures that all voxels within damping zone 1 shown in Fig. 2(a) are below 3.78 mm in dimension. Using the criteria mentioned by Bres [39] which states that each acoustic wavelength should be resolved by at least 12 computational cells, this setup is able to resolve at least up to 8400 Hz with proper levels of numerical dissipation up to the microphone locations. The number of voxels used for each case is summed up in Table 1.

2.3. Boundary conditions and initialization

In the 2D DNS Lips, 3D DNS and 3D DNS-SLR cases, an inlet velocity profile is used with slip conditions on the walls of the wind tunnel lips in order to match the velocity measurements of Neal et al. [25] at the outlet plane of the wind tunnel. For the 3D DNS-SLRT case, a uniform inlet velocity is used to impose equal volumetric flow rate to the previous 4 cases. On the other hand, the 2D DNS Free-field case uses an uniform inlet velocity U_∞ of 16 m/s. Fig. 5 shows the nozzle exit velocity profiles taken at $X/L_w = 0$ made dimensionless by U_{ref} which is the maximum velocity in the profile and reported in Table 1. All velocity profiles compare well with measurement. All nozzle cases have a coflow of 0.165 m/s to mimic the actual flow entrainment in the wind tunnel. Dirichlet boundary conditions based on pressure are imposed on all outlets while no slip boundary conditions are implemented on the airfoil. Furthermore, to avoid reflection at the outlets and to mimic anechoic conditions, air viscosity is artificially increased in Damping Zones 1 and 2 in order to mimic the behavior of anechoic walls as shown in Fig. 2(a). This is accomplished by controlling $\frac{\nu^*}{T^*}$ where ν^* is the dimensionless kinematic viscosity and T^* is the lattice temperature [40]. By imposing this ratio to 0.01 in damping zone 1 and 0.2 in damping zone 2, the physical viscosity is progressively increased in these 2 regions in order to damp out sound waves traveling away from the airfoil [35].

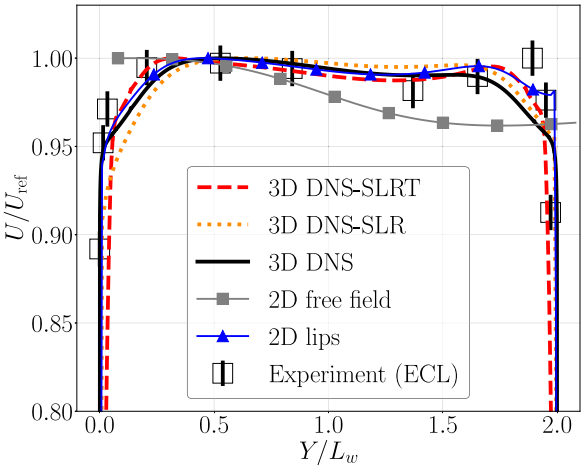

Fig. 5. Velocity Magnitude profile at outlet plane of the wind tunnel nozzle ($X/L_w = 0$). Experimental results from ECL [25] are shown with error bars.

In order to shorten the time to reach statistical convergence, initialization for the 3D DNS case has been performed using 2D DNS simulation results. Simulations of the 3D DNS-SLR and 3D DNS-SLRT case were initialized using results from the 3D DNS case. Thereafter, cases were run for at least 26 through flow times where a through flow time is defined as c/U_∞. Subsequently, only the final 20 through flow times are used during post-processing. Note that the number of through flow times is significantly increased from the previous studies in [8,11,26], which only used 5–6 through flow times to establish the turbulent flow statistics around the airfoil. This was necessary in order to establish the coupling between the airfoil and the wind tunnel shear layer which will be elaborated upon in the following sections. In total, each case took 90 h on 1440 Intel "Skylake" cores at 2.4 GHz. Furthermore, the 3D DNS-SLRT case was extended to reach a total of 80 through flow times to capture several periods of the LSB movement. This took a total of 317 h with the same number of cores.

3. Aerodynamic results

3.1. Flow topology

Fig. 6 shows the overall flow regime in the wind tunnel nozzle and provides two consecutive zooms on the airfoil stressing the boundary-layer developments, and at the airfoil leading edge emphasizing the transition process, respectively.

By comparing 3D DNS with 3D DNS-SLR in Fig. 6, the refinement of the shear layers is seen to drastically change the structure of the shear layer upstream of the airfoil. On the one hand, in the 2D DNS Lips and in the 3D DNS cases the jet shear layer remained laminar up to the mid chord of the CD airfoil before forming Kelvin–Helmholtz instabilities and transitioning to turbulence. On the other hand, in the 3D DNS-SLR case with additional refinement, the development of Kelvin–Helmholtz instabilities started from the nozzle lip. This caused vortex pairing right above the leading edge of the airfoil. Because of the turbulent state of the boundary layer achieved at the nozzle exit, the large instabilities in the shear layers are eliminated, postponing the vortex pairing further downstream after the trailing-edge.

Significant differences in flow topology exist between the airfoil flow regimes of 2D and 3D simulations. Starting with the 2D cases, the zoom over the whole airfoil shows that in the 2D DNS free field setup the suction-side boundary layer is turbulent from the leading edge and begins to detach near midchord. The turbulent boundary layer remains attached in all the cases where the wind tunnel nozzle lip was included as seen in 3D DNS, 3D DNS-SLR, 3D DNS-SLRT and the 2D DNS Lips cases. Furthermore, large coherent perturbations can be seen in the 2D DNS Free-field case that start from the leading edge and persist to the trailing edge due to the lack of vortex stretching and dissipation in the spanwise direction. In the 2D DNS Lips case the coherent structures are smaller and remain attached until the trailing edge. Note that another difference between the 2D cases can be seen in the leading edge zoom which shows that the stagnation point in the 2D DNS Free-field setup is slightly shifted toward the pressure side compared to the 2D DNS Lips. Indeed, the jet confinement modifies the effective angle of attack as mentioned for instance by Brooks et al. [41] and Sanjose et al. [11]. Yet, no simple incidence correction applies to the CD airfoil to properly match the free-field pressure distribution [19,42]. In contrast to the behavior observed in 2D cases, the coherent structures in 3D cases undergo dissipation to smaller scales beyond the reattachment point, as illustrated in the 3D DNS, 3D DNS-SLR and 3D DNS-SLRT cases.

A detailed view of the flow topology of the airfoil and the wind tunnel in the 3D cases can be obtained using the λ_2 criterion [43]. The airfoil flow topologies of the 3D DNS-SLRT and 3D DNS-SLR cases are similar to the 3D DNS case so only the 3D DNS result will be shown here (see Fig. 7). The result is similar to that of [9,28]. In these simulations, the CD airfoil at $\alpha = 8°$ is seen to have a LSB at the leading edge which transitions to turbulence and triggers an attached turbulent boundary layer which convects over the trailing edge. A forest of hairpin vortices develop after the LSB on the suction side. The pressure side remains laminar up to the trailing edge with a small vortex shedding as observed in previous high-fidelity simulations.

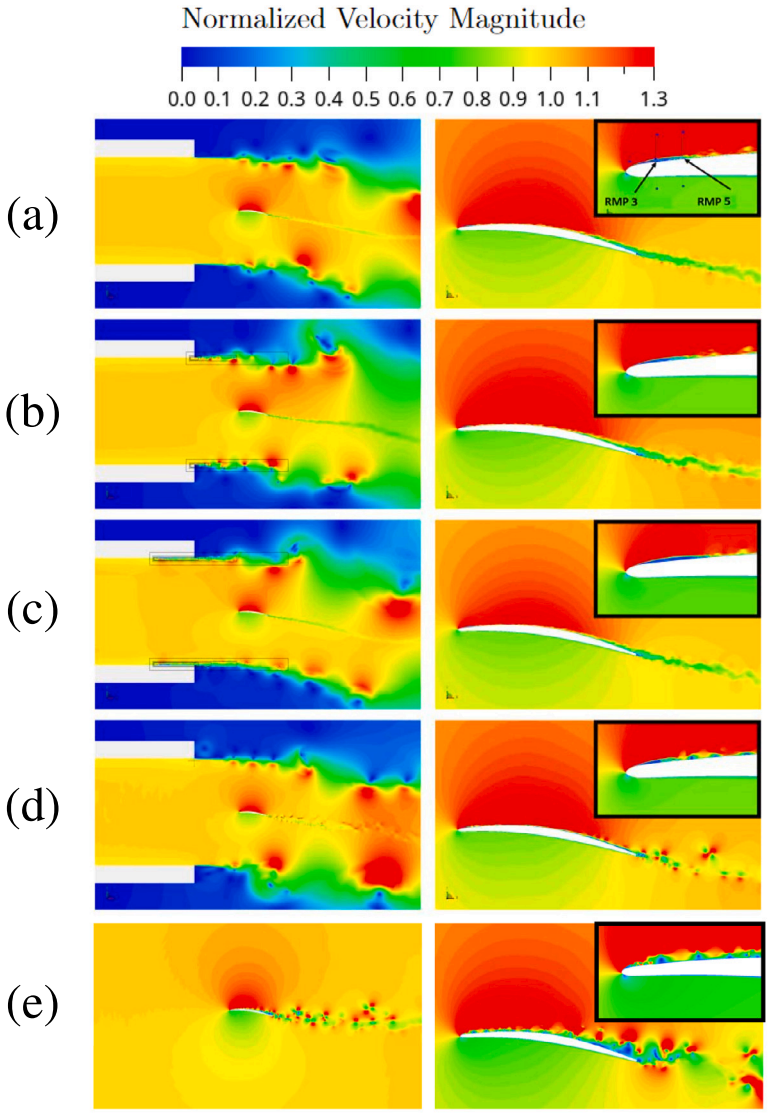

Fig. 6. Midplane contours of instantaneous velocity magnitude normalized by mean inlet velocity. (a) 3D DNS, (b) 3D DNS-SLR, (c) 3D DNS-SLRT, (d) 2D lips and (e) 2D Free-field.

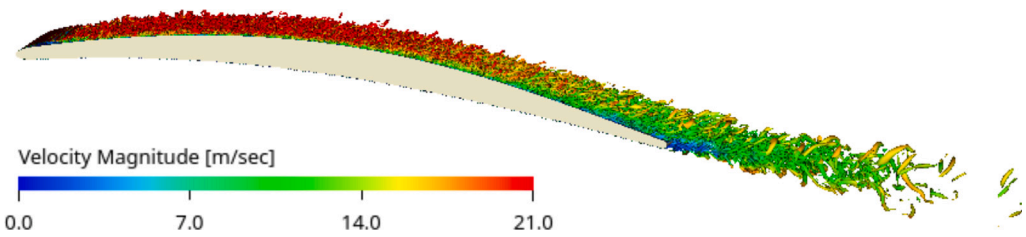

Fig. 7. Isosurface of $\lambda_2 = -1 \times 10^7$ near the surface of the airfoil (colored by velocity magnitude). (For interpretation of the references to color in this figure legend, the reader is referred to the web version of this article.)

The λ_2 criterion is plotted near the wind tunnel lips for the 3D cases in Fig. 8. Evidently grid refinement resulted in the development of spanwise coherent structures which are seen in the 3D DNS-SLR case but not in the 3D DNS case. In the 3D DNS-SLRT simulation where the flow is tripped, the exiting flow of the wind tunnel is fully turbulent. The resulting unsteadiness in the flow exiting the wind tunnel may be quantified by turbulence intensity upstream of the airfoil as shown in Fig. 9, which is defined as

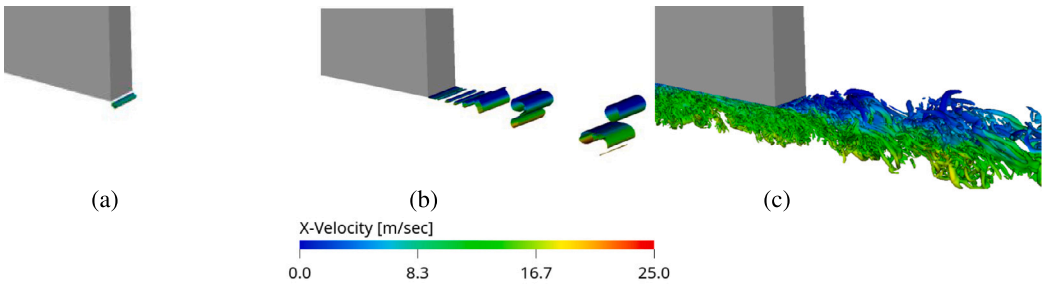

Fig. 8. λ_2 criterion at wind tunnel nozzle lip (colored by x-velocity). (a) DNS, (b) DNS-SLR and (c) DNS-SLRT. (For interpretation of the references to color in this figure legend, the reader is referred to the web version of this article.)

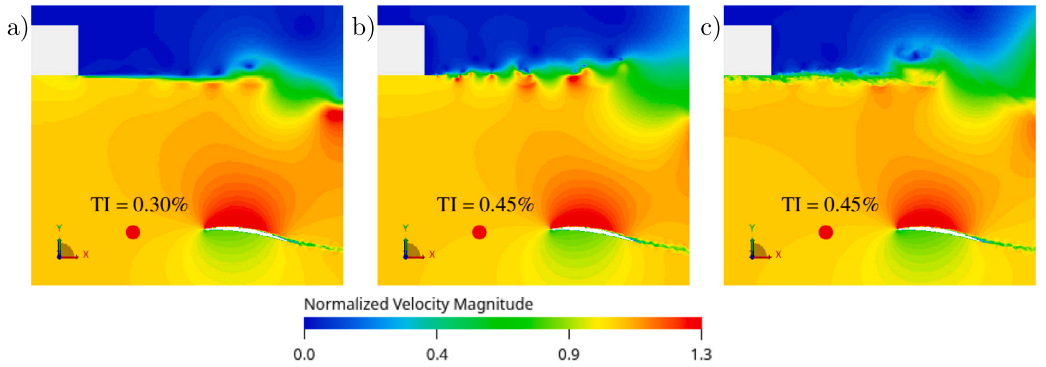

Fig. 9. Detailed view of shear layer and Turbulence Intensity (TI) observed at $x/c = -2$ for (a) 3D DNS, (b) 3D DNS-SLR, (c) 3D DNS-SLRT.

u'/U where u' is the root-mean-square of the streamwise velocity fluctuation and U is the mean streamwise velocity magnitude. The turbulence intensity of the 3D DNS case is 0.30% and it is taken at $x/c = -2$. For both 3D DNS-SLR and 3D DNS-SLRT cases, this turbulence intensity has increased to 0.45%. This is most likely caused by the fluctuations forming upstream of the airfoil leading edge in both simulations due to the refined voxels in the wind tunnel shear layer. This brings it closer to the experimentally measured value of 0.7% at ECL [25], and of 0.4% at UdeS [16]. This stresses the key role of the shear layer at the nozzle lip for the first time: it can generate turbulent fluctuations within the jet potential core that modify the level of turbulence seen by the airfoil and generate an extra turbulence-interaction noise mechanism at the airfoil leading edge. Note that the present study has not investigated the effect of length scales of inlet turbulence and this may play a role in influencing the flow over the airfoil [44].

3.2. Mean flow

3.2.1. Mean wall-pressure coefficient

Now that the instantaneous flow topology has been described in the previous sections, it is of interest to study the mean flow of the airfoil. The mean aerodynamic loading on the airfoil is quantified by the mean wall-pressure coefficient, $\overline{C_p}$, which is defined as

$$\overline{C_p} = \frac{\overline{p} - p_{\text{ref}}}{\frac{1}{2}\rho_{\text{ref}} U_{\text{ref}}^2} \tag{1}$$

where p_{ref}, ρ_{ref} and U_{ref} are the reference pressure, density and velocity respectively, taken at the exit of the nozzle. The results of $\overline{C_p}$ from the five simulations are shown in Fig. 10. These numerical results are compared with experimental results measured at UdeS [45] and ECL [25]. At first glance, the $\overline{C_p}$ obtained in the 2D DNS free field case deviates from all other results, particularly in the intensity of the LSB, as indicated by the pronounced steepness observed in the region characterized by highly negative $\overline{C_p}$ values. For the 3D cases the mean effect of the shear layer refinement and transition to turbulence in the wind tunnel nozzle lips is seen to reduce the size of the LSB at the first 10% of the airfoil. This may be explained by the increase in turbulence intensity from 0.30% to 0.45% from 3D DNS to 3D DNS-SLRT and 3D DNS-SLR. This agrees well with previous observations on the NACA0018 airfoil at a similar chord Reynolds number by Istvan et al. [46].

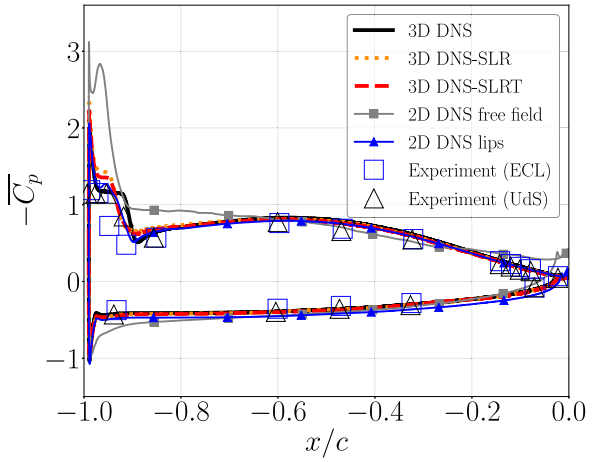

Fig. 10. Mean wall-pressure coefficient along the chord length of the CD airfoil.

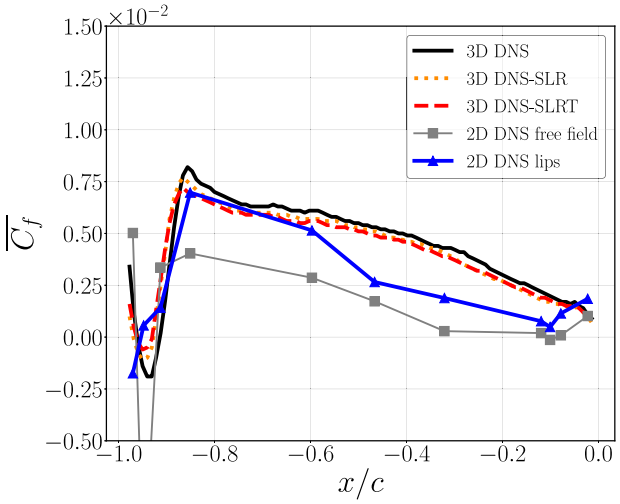

Fig. 11. Mean friction coefficient along the chord length of the CD airfoil.

3.2.2. Mean friction coefficient

A more detailed examination of the LSB may be obtained from the mean friction coefficient, $\overline{C_f}$ defined by:

$$\overline{C_f} = \frac{\overline{\tau}}{\frac{1}{2}\rho_{\text{ref}} U_{\text{ref}}^2} \tag{2}$$

$\overline{C_f}$ for all DNS is compared in Fig. 11. The mean reattachment location of the separation bubble may be inferred from the location where $\overline{C_f}$ first crosses the line that represents $\overline{C_f} = 0$. Using this criteria, it can be seen that both the 3D DNS-SLRT and 3D DNS-SLR cases have mean reattachment locations which are further upstream than in the 3D DNS case, which is consistent with the shorter plateaus observed in Fig. 10. This is also the case of the 2D DNS Lips simulation, but with a sharper decay of $\overline{C_f}$ after mid-chord in the adverse pressure gradient region with almost a flow separation at the trailing edge. Finally, the 2D DNS Free-field simulation does not only exhibit an intense flow separation at the leading edge, but also a marked one at the 90% chord, again stressing the very different flow regime for this case.

3.2.3. Boundary layer profile

Fig. 12 compares all DNS results with hot-wire measurements [25], and shows the effect of the wind tunnel jet on the airfoil flow regime. From the velocity profile above RMP 5, the 3D DNS-SLR and 3D DNS-SLRT are seen to show similar results while kinks are present in the velocity profiles of the reference 3D DNS. This is most likely an effect of the earlier reattachment of the LSB seen in Fig. 11. At the other downstream probe locations, boundary layer profiles are similar between simulation and experiment. For the 2D cases, the boundary layer profiles show that the 2D DNS Free-field case has flow detachment at RMPs 21 and 25 (consistently with Fig. 11), while the 2D DNS Lips case has attached flow at these locations.

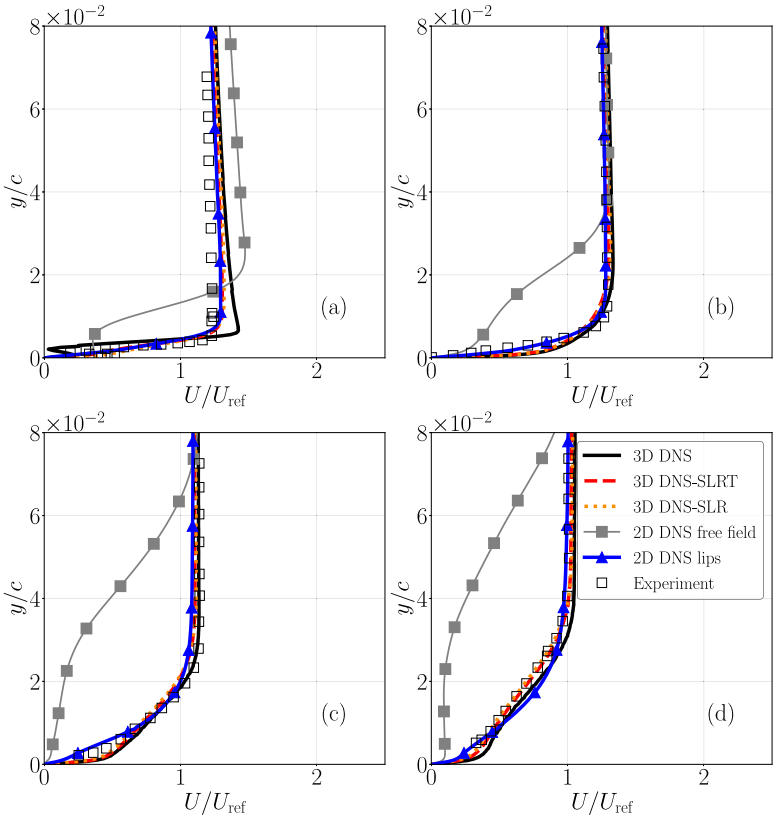

Fig. 12. Velocity magnitude at different RMP locations on the airfoil suction side: (a) RMP 5, (b) RMP 9, (c) RMP 21, (d) RMP 25.

3.2.4. Wind tunnel shear layer

Finally, a comparison between the velocity magnitudes measured close to the nozzle lips in ECL [25] and the simulation results is performed for the first time. In Fig. 13, some noticeable discrepancies still exist between all five DNS and experiment. However, the 3D DNS-SLRT case provides better overall agreement with experimental results than the 3D DNS-SLR and 2D DNS Lips cases, and particularly at $X/L_w = 1.36$ above the trailing edge of the airfoil. Moreover, none of the profiles match the experimental results near the nozzle exit at $X/L_w = 0.008$. It can be inferred from this result that the profile at the nozzle exit in the experiment lies between a laminar and a fully turbulent state, which is not entirely captured in the five simulations. Note, this is most likely a source of uncertainty in open jet test facilities [25,47] that have different converging sections and contractions, and upstream turbulence levels. This could explain the current large variations seen in the noise levels reported on the NACA0012 airfoil (Fig. 11 in [18]).

3.3. Unsteady flow

3.3.1. Probability density function of pressure coefficient

Wall-pressure fluctuations offer a valuable means to visualize the influence of grid refinement of wind tunnel shear layer on surface loading. A contour plot of the normalized probability density function (PDF) of C_p is shown in Fig. 14 (left column). A careful examination of the PDF plots reveals mostly notable variations in the LSB region before the reattachment point. Moreover, different LSB behavior results from differences in the development of the wind tunnel shear layer. This is particularly visible in the 3D DNS-SLR case (Fig. 14(c)). The refinement leads to an earlier reattachment of the LSB shear layer and a sharper pressure drop in pressure at the reattachment point. Additionally, in the 3D DNS-SLRT case (Fig. 14(e)), earlier instabilities near the leading edge of the airfoil are promoted. The change in behavior of the LSB is further illustrated through iso-contours of λ_2 criterion shown in Fig. 15. The reference DNS case (Fig. 15(a)) shows a longer roll-up region behind the initial flow separation of the laminar boundary layer than the 3D DNS-SLRT case (Fig. 15(b)). This provides further evidence that the overall effect of the changes made in 3D DNS-SLRT is to speed up transition to turbulent boundary layer flow near the leading edge.

3.3.2. Probability density function of friction coefficient

The fluctuations in wall shear exhibit a pattern similar to that observed in pressure fluctuations with most variations in the LSB. The latter grows when the transition starts and gets damped after the re-attachment point. Some differences are also induced by the various jet shear-layer development. Furthermore, by examining the normalized PDF of C_f zoomed in this region in Fig. 14

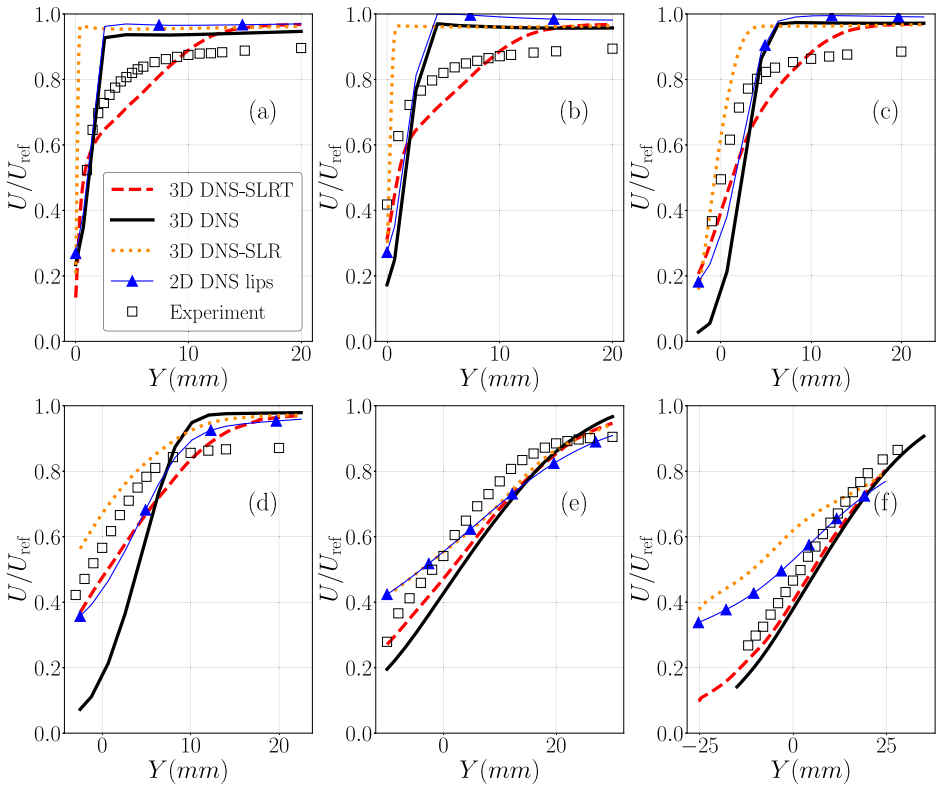

Fig. 13. Profiles of velocity magnitude at positions downstream of nozzle exit lip: (a) $X/L_w = 0.008$, (b) $X/L_w = 0.04$, (c) $X/L_w = 0.12$, (d) $X/L_w = 0.44$, (e) $X/L_w = 1.04$, (f) $X/L_w = 1.36$.

(right column), the point at which C_f transitions from a negative to a positive value indicates the instantaneous location of the LSB reattachment. Isovalue lines of PDF = 0.25 reveal that, for the 3D DNS case (Fig. 14(b)), the reattachment position fluctuates between approximately $x/c = -0.950$ and $x/c = -0.895$. In the 3D DNS-SLR (Fig. 14(d)) and 3D DNS-SLRT cases (Fig. 14(f)), where the wind tunnel shear layer becomes more unsteady, the reattachment location not only exhibits a broader range of variation but also shifts closer to the leading edge. Finally, it should be stressed these variations of C_f on this airfoil at this particular operating condition are very similar both in terms of shape and amplitude to those reported in [28].

3.3.3. Airfoil-wind tunnel interaction

Now that the differences in flow regime on the airfoil due to changes in the wind tunnel shear layer have been established, the level of correlation which exists between the two areas of interest can first be quantified. This original assessment provides a further step towards inferring causal links between the fluid phenomena happening on the airfoil and that which happens inside the jet shear layer. This study has been performed on the 3D DNS-SLRT case as it provides a more physical representation of the flow at the nozzle exit (notably the shear layer in Fig. 13). The cross-correlation between the following 3 quantities is then computed for the 3D DNS-SLRT case :

- **A.** α_i, which is the instantaneous change in angle of attack relative to α. α_i is computed as $\alpha_i = \arctan\left(\frac{v'}{u'}\right)$ at the location 0.6 c upstream of the LE, labeled 'AoA probe' in Fig. 16.
- **B.** x_{LSB}, which is the reattachment point of the LSB near the leading edge. This is the point at which C_f changes from a negative to a positive value. ($x_{\mathrm{LSB}} = -1.0$ refers to the leading edge and $x_{\mathrm{LSB}} = 0.0$ refers to the TE)
- **C.** v', which is the crosswise velocity fluctuation observed at 6 different positions (labeled as Probe 6 to Probe 38 in Fig. 16) within the wind tunnel jet shear layer.

The correlation coefficient as defined in [48] is used. This is given for 2 variables ζ and χ at 2 locations (x, y, z) and (x', y', z') by

$$R_{\zeta\chi}(x, x', y, y', z, z') = \frac{\overline{\zeta(x, y, z)\chi(x', y', z')}}{\sqrt{\overline{\zeta^2(x, y, z)}}\sqrt{\overline{\chi^2(x', y', z')}}} \tag{3}$$

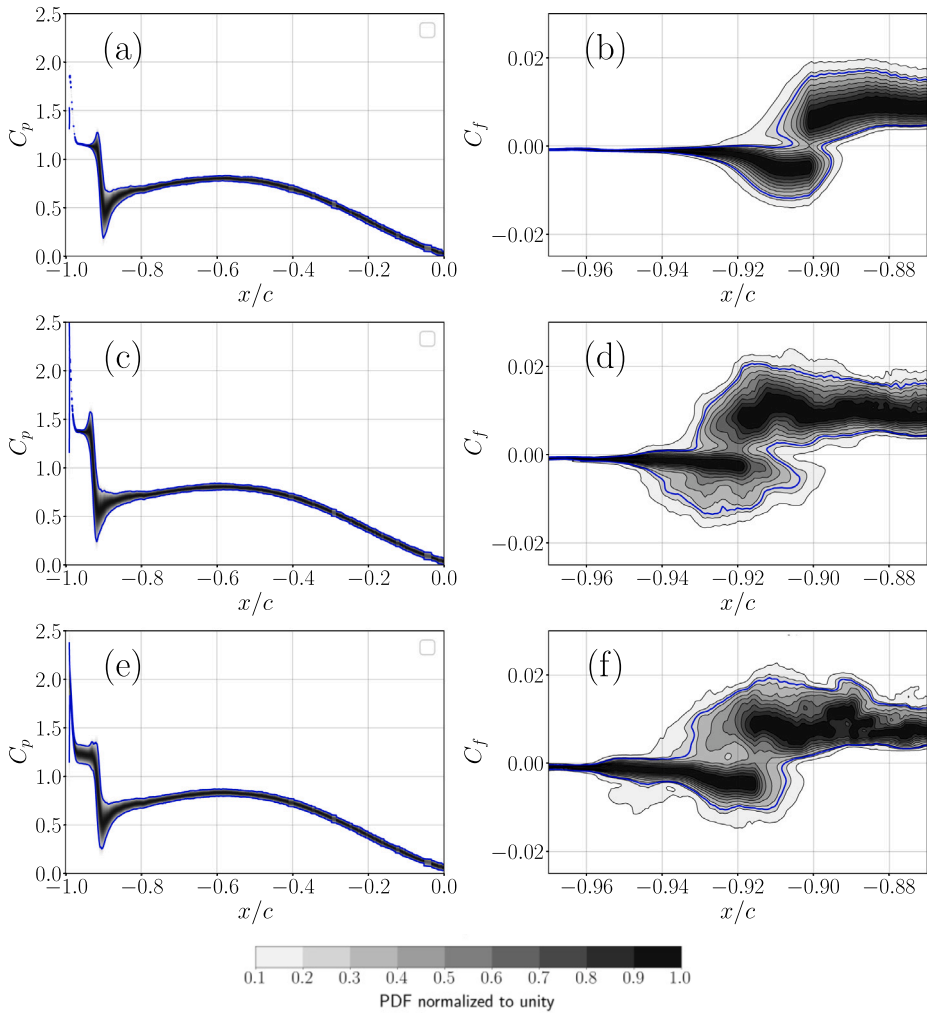

Fig. 14. Normalized PDF of C_p (left column) and C_f (right column). Blue lines indicate where PDF = 0.25. (a–b): 3D DNS, (c–d): 3D DNS-SLRT, (e–f): 3D DNS-SLRT. (For interpretation of the references to color in this figure legend, the reader is referred to the web version of this article.)

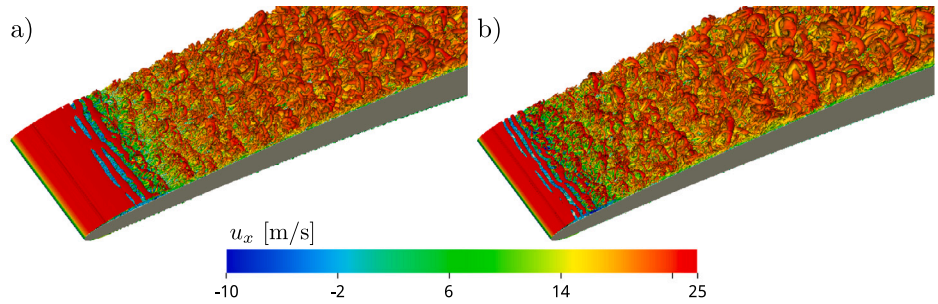

Fig. 15. Isosurface of λ_2 criterion close to the airfoil, colored by x velocity: (a) 3D DNS, (b) 3D DNS-SLRT. (For interpretation of the references to color in this figure legend, the reader is referred to the web version of this article.)

The cross-correlation between α_i and x_{LSB} is first shown in Fig. 17(a). A strong positive correlation is seen to exist between the two quantities and an increase in α_i is associated with a shortening of the LSB (decrease in x_{LSB}). Next, the correlation between α_i and v' at 3 locations in the wind tunnel shear layer is computed and shown in Fig. 17(b). A weak correlation is found near the nozzle lip where the emerging separated shear layer contains only small turbulent structures. Further downstream where larger vortices are formed, higher correlation between the downstream probe (probe 38) and α_i is seen. This shows that the pairing of the

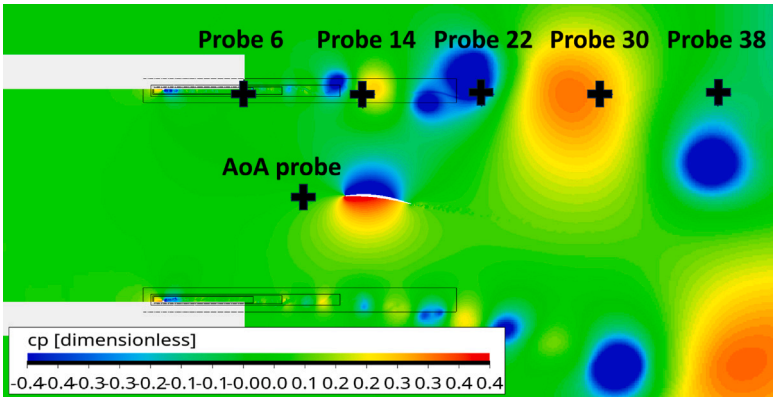

Fig. 16. Locations of the probes used for measuring correlation and contours of pressure coefficient.

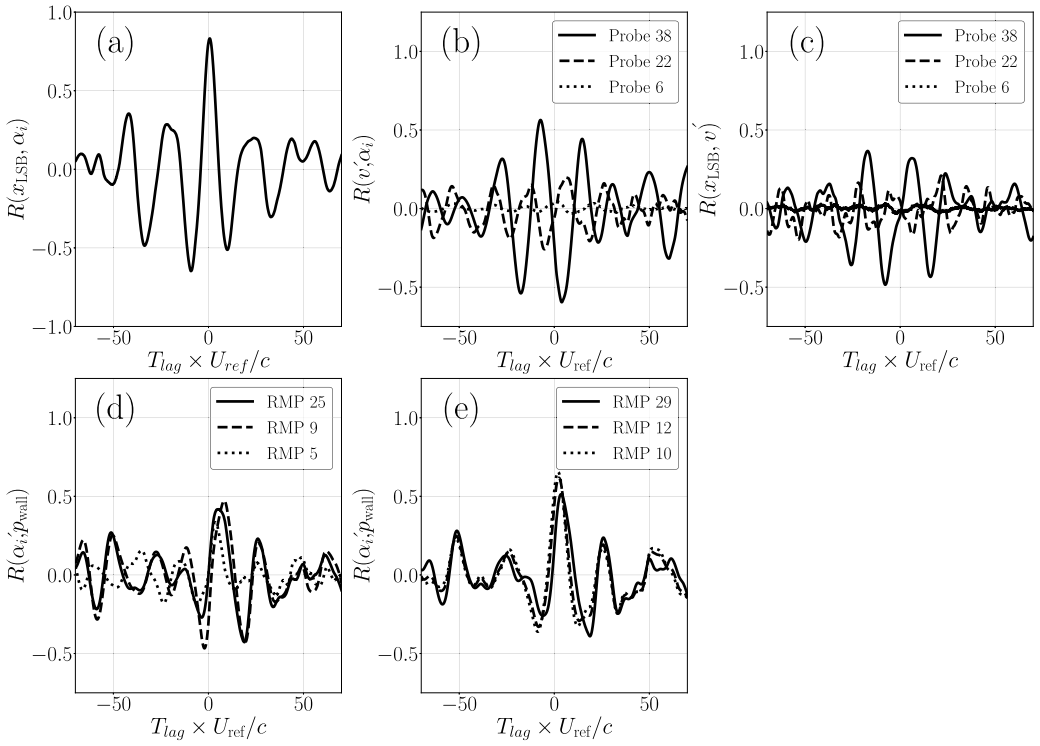

Fig. 17. Cross correlation between different parameters in the jet potential core (a) α_i and x_{LSB}, (b) α_i and shear layer v', (c) x_{LSB} and shear layer v', (d) α_i and RMP on the suction side and (e) α_i and RMP on the pressure side.

large scale vortices in the shear layer is correlated with instantaneous changes in α_i. In order to identify if the reattachment point and the shear layer are coupled, cross-correlation is performed between the reattachment point and v' at the 3 shear layer probes. As shown in Fig. 17(c), correlation is high between v' at probe 38 and x_{LSB}.

In order to determine if the shear layer motions affect wall-pressure fluctuations, Fig. 17(d) and (e) show cross correlations between α_i and $p'(\mathbf{x}, t)$ on the airfoil in the 3D DNS-SLRT case for RMP locations on both the suction and pressure sides of the airfoil shown in Fig. 1. As mentioned in [49], the pressure fluctuations on the pressure side represent the scattered pressure generated by the convection of turbulence on the airfoil suction side over the trailing edge. Both scattered and incident pressure are clearly shaped by the unsteady loading caused by oscillations of α_i. According to Amiet's model [50,51], this is expected to have direct implications on the trailing-edge noise generated.

In summary, the instantaneous change of angle of attack α_i has a direct and strong influence on the LSB size. The fluctuations in α_i are, in turn, influenced by the large-scale movement of the jet shear layer which also drives the fluctuations of v' observed at

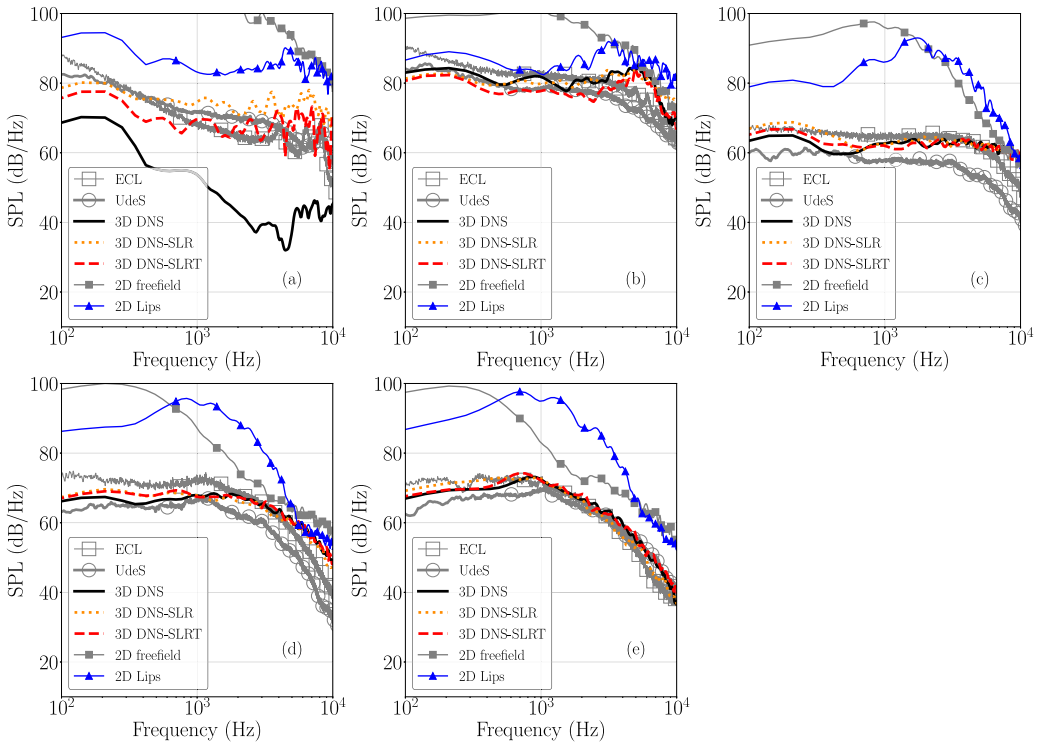

Fig. 18. PSD of wall-pressure fluctuations at different chordwise locations. (a) RMP 3, (b) RMP 5, (c) RMP 9, (d) RMP 21, (e) RMP 25.

the probe far downstream. Furthermore, the pressure footprint caused by this jet shear-layer movement persists on both the suction and pressure sides of the airfoil.

3.3.4. Wall-pressure spectra

Wall-pressure spectra are expected to provide some insight into the airfoil noise sources. This is checked at the RMP locations shown in Fig. 1, and compared in Fig. 18 for all simulations to look at both 2D versus 3D DNS and the effect of the resolved shear layer in wind tunnel simulations. A Welch periodogram method is applied using 26 Hanning windows with 50% overlap.

Firstly, all 2D results show overpredicted wall-pressure spectra when compared with experimental results. On the one hand, the 2D DNS Free-field case has the largest slope with a shape that is closer to detached flow as reported experimentally at 15° geometrical angle of attack [15,48]. This is consistent with the flow patterns found in Fig. 6 for the 2D DNS Free-field case, which can be qualitatively compared to the Particle Image Velocimetry results in [48]. On the other hand, the 2D DNS Lips results are much closer to experiment near the leading edge within the LSB (similar flow behavior shown in Fig. 6). Yet, further downstream in the adverse pressure gradient region after the airfoil mid-chord, the turbulent eddies that cannot stretch in the spanwise direction are far too energetic and coherent, and yield a large hump centered on about 1 kHz, sign of strong vortex shedding. This confirms that an unrealistic development of turbulence over the airfoil takes place in the 2D cases, and consequently improper noise sources (direct overprediction of the noise levels based on Amiet's model for instance).

On the other hand 3D results show far better agreement with experiments. In Fig. 18(a), at RMP 3, which is located within the LSB, higher levels of Power Spectral Density (PSD) are seen in 3D DNS-SLR and in 3D DNS-SLRT than in the 3D DNS. This offers a closer match to UdeS and ECL results. The reason for this is likely to be that the point of transition to turbulence and consequent reattachment of the LSB moves back and forth between RMP 3 and RMP 5 and that this does not happen in the 3D DNS case. This observation is similar to a previous observation by Istvan et al. [46], which showed that increased background turbulence intensity moved the mean location of flow reattachment upstream on airfoils at moderate Reynolds numbers. Moreover, in Fig. 18(b), at RMP 5, 3D simulation results capture a hump at high frequencies which is not present in experimental results. This suggests that the effects of vortex shedding associated with the laminar flow separation [15] is still significant at this probe location in the simulations (seen in Fig. 6). At the downstream locations near the trailing edge, in Fig. 18(d), at RMP 21, the turbulent boundary layer becomes fully developed for all three simulations and the wall-pressure spectra become similar. However, a sharper decay of the PSD is observed in experiment. Nevertheless, in Fig. 18(e), at RMP 25 which is closest to the trailing edge, wall-pressure spectra are similar for all 3D simulations and experiment.

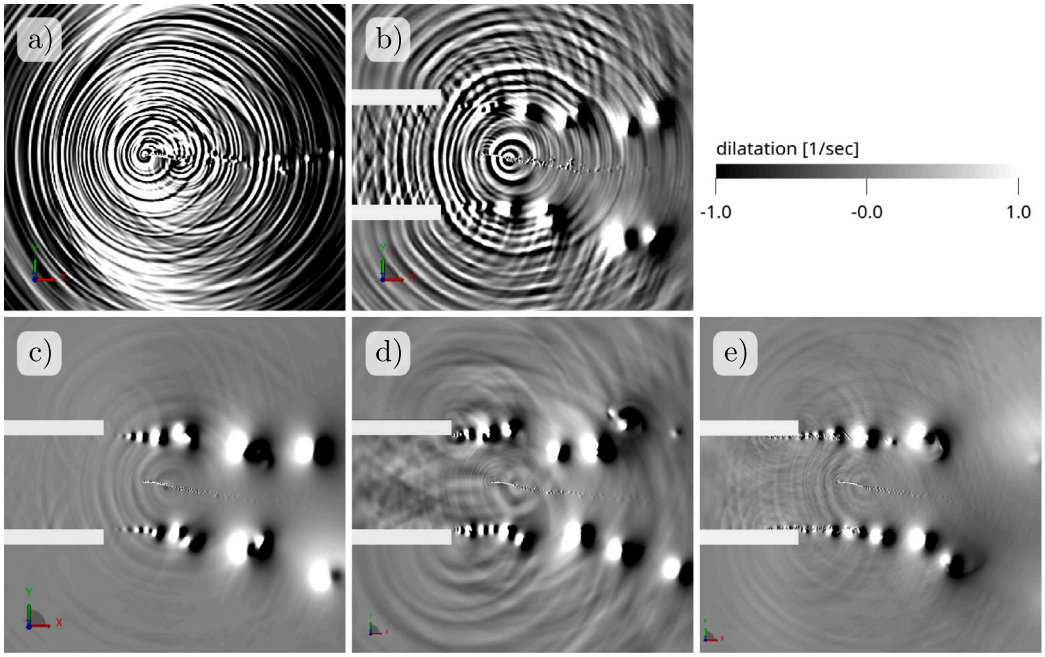

Fig. 19. Midspan contours of dilatation defined as $\frac{1}{\rho}\frac{\partial \rho}{\partial t}$ for (a) 2D DNS Free field, (b) 2D DNS Lips, (c) 3D DNS, (d) 3D DNS-SLR and (e) 3D DNS-SLRT.

4. Aeroacoustic results

4.1. Dilatation field

To visualize the noise sources, contours of dilatation field are plotted in Fig. 19 for all cases. In the 2D DNS Free-field case (Fig. 19(a)), the dilatation field is dominated by wavefronts radiating from the leading edge. In the 2D DNS Lips case (Fig. 19(b)), this source is attenuated and is less prominent than the trailing edge noise source which appears in both configurations and this is likely due to the jet confinement effect.

3D cases show evidence of trailing edge and leading edge LSB noise as well. In addition to these, the vortex pairing events near the lips also form a noise source in the 3D DNS-SLR case (Fig. 19(d)), due to increased activity in the shear layer due to grid refinement in that region. When the zigzag trip was added in the 3D DNS-SLRT case (Fig. 19(e)), this jet source strongly diffracting at the nozzle lips was largely attenuated. Yet, the trip in the latter simulation introduces a new weaker spurious noise source at high frequency (smaller wavelength). In all 3D cases, both the leading edge LSB and trailing edge turbulent eddies are significant emitters of noise as found previously [9,28], and it is of interest to investigate the role of the wind tunnel shear layer in influencing the balance between these two noise sources.

To illustrate this, the instantaneous change of geometric angle of attack, α_i, with time is first given in Fig. 20. Dilatation plots in the time interval $0.38\ \text{s} < t < 0.51\ \text{s}$ are given in Fig. 21. Within this time interval, a transition in the variation of angle of attack is observed, decreasing from 2.5° to 0.6° and then increasing to 3.2°. These changes in α_i correspond to notable variations in the nature of noise sources, as depicted in Fig. 21. At $t = 0.384$ s (Fig. 21(a)), marked by the red cross in Fig. 20 and corresponding to $\alpha_i = 2.5°$, both a LSB and a trailing-edge noise sources are present as seen from the two sets of dilatation contours centered on the trailing edge and leading edge. By $t = 0.410$ s (Fig. 21(b)), the LSB source diminishes. Finally, at $t = 0.435$ s (Fig. 21(c)), when $\alpha_i = 0.6°$ (marked by the blue dot in Fig. 20), the LSB source becomes nearly non-existent, leaving only the trailing edge noise source. Subsequently, after $t = 0.435$ s, there is a resurgence in α_i to a peak of 3.2°. Concurrently, as α_i increases again, the LSB noise source intensifies, as evidenced in Fig. 21(d) to (f). It is therefore apparent that this 'switching' in the level of LSB activity caused by the change in α_i is responsible for modulating the amplitude of the leading edge noise source.

Band-pass filtering on the dilatation field to extract the filtered dilatation field between the frequencies of 5000 Hz to 7000 Hz. is shown in Fig. 22(a). The main noise contributor in this frequency range is seen to be the LSB. A closer look may be obtained by overlaying the dilatation field of the final time frame with the isosurface of the λ_2 criterion. As seen in Fig. 22(b), the noise comes from the region in which the separated laminar flow from the LSB reattaches and transitions to turbulence thereby confirming the role of the LSB in noise generation near the leading edge in this frequency range.

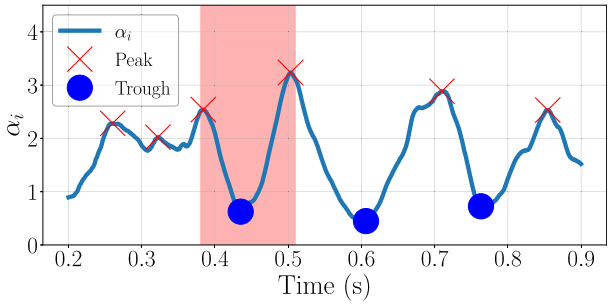

Fig. 20. α_i vs. time. Peaks (red) and troughs (blue) are marked. (For interpretation of the references to color in this figure legend, the reader is referred to the web version of this article.)

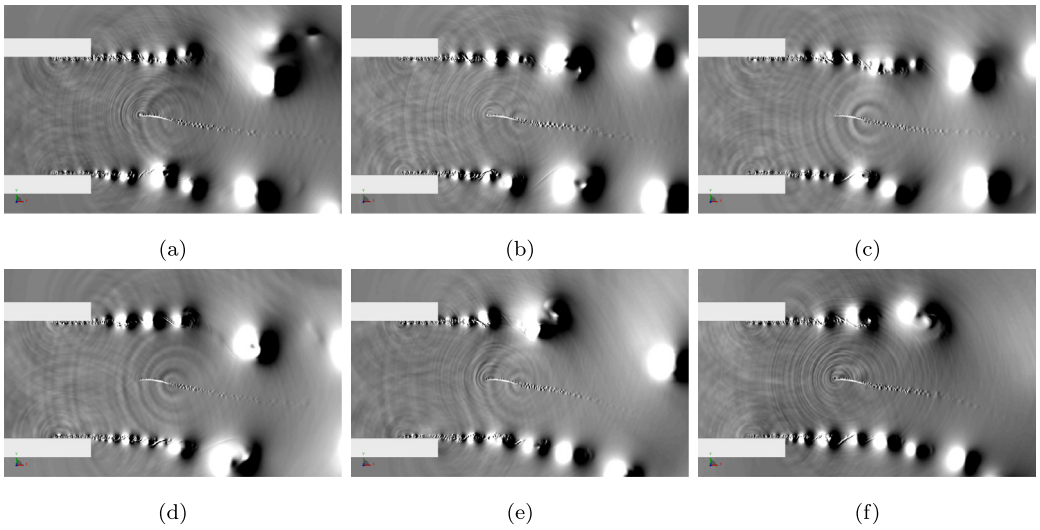

Fig. 21. Evolution of instantaneous dilatation with time. (a) t = 0.384 s, (b) t = 0.410 s, (c) t = 0.435 s, (d) t = 0.461 s, (e) t = 0.486 s and (f) t = 0.504 s.

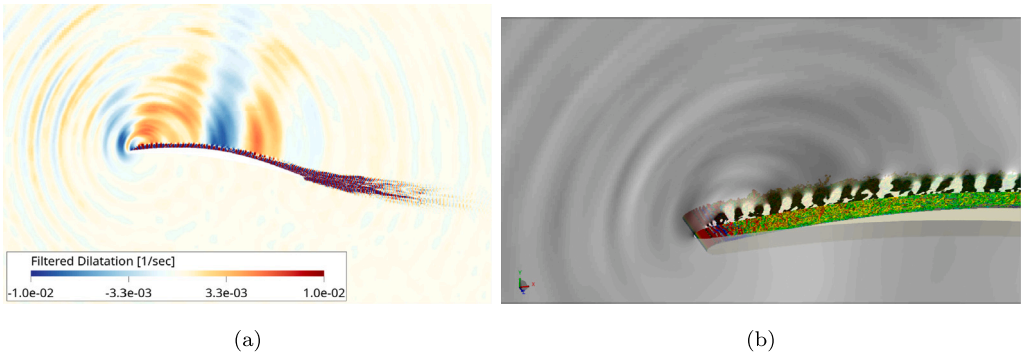

Fig. 22. Midspan dilatation field band-pass filtered from 5000 Hz to 7500 Hz (a) and superimposed on isosurface of λ_2 (b).

4.2. Acoustic spectra

For a quantitative look at the effect of a better resolution of the jet shear layer and of the zigzag trip on the far-field noise, PSD of the far-field acoustic pressure are compared with the measurements achieved at UdeS [52] and ECL [25]. The latter, taken at 2 m from the airfoil trailing edge and at 90° above the suction side, is represented by the black line in Fig. 23. The experimental results measured at 1.21 m are scaled to 2 m using the far-field spherical wave assumption. The same scaling method, as described by Sanjose et al. [53], is also used for the direct noise numerical predictions, which were taken from a probe 0.45 m above the trailing edge. In addition, a Mach number scaling (to account for the discrepancy between simulated Mach number $M_{\text{sim}} = 0.2$ and

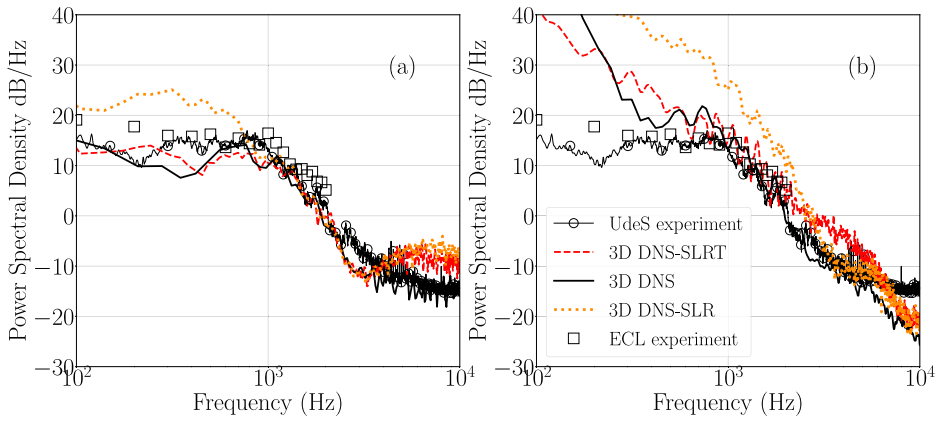

Fig. 23. Farfield noise computed using (a) FWH analogy and (b) Direct simulation.

experimental Mach number $M_{exp} = 0.05$) and a span-width extent scaling (to account for the difference between simulated span width of $L_{sim} = 1.5$ cm and experimental span width of $L_{exp} = 30$ cm) is applied to direct noise results in order to correct simulation results for experimental conditions. These corrections are summarized in Eq. (4).

$$S_{pp}^{corr} = S_{pp}^{3Dsim} \frac{R_{sim}^2}{R_{exp}^2} \frac{L_{exp}}{L_{sim}} \frac{M_{exp}}{M_{sim}} \tag{4}$$

On the other hand, in Fig. 23(a), the acoustic pressure at 2 m is calculated from surface pressure fluctuations on the airfoil using the Ffowcs Williams and Hawkings' analogy (FWH) with the in-house code SherFWH [9,13,35]. The numerical PSD are computed using Welch's periodogram method by dividing the direct pressure signals into 12 blocks and the FWH results into 16 time blocks using a Hanning window with 50% overlap.

From Direct Noise results shown in Fig. 23(b), the combined effect of refining the shear layer grid and adding the zigzag trip (3D DNS-SLRT) can be seen to give a similar result to the 3D DNS. The over-prediction below 300 Hz is most likely caused by the influence of vortex pairing happening in the under-resolved parts of the jet shear layer [54]. In the simulation in which no trip was added (3D DNS-SLR), this effect seems to be strengthened, causing over-predictions below 2000 Hz as seen in Fig. 23(a). This is consistent with the iso-contours of velocity magnitude in Fig. 6 for the 3D DNS-SLR case, which show a much earlier and stronger jet vortex pairing.

From SherFWH results in Fig. 23(a), 3D DNS and 3D DNS-SLRT agree with experimental results below 4000 Hz. At frequencies above 4000 Hz, a hump is seen in simulations with shear-layer refinement (3D DNS-SLR and 3D DNS-SLRT), which was not as marked in the experiment (rather a plateau well captured by the 3D DNS). Referring back to the band-pass filtered dilatation result in Fig. 22(a), it is likely that the hump seen in the SherFWH results originates from the high wall-pressure fluctuations near the LSB. A similar high-frequency hump was seen in the DNS results of Wu et al. [9]. Note also that the 3D DNS-SLR simulation sees a low frequency over-prediction that is likely related to the footprint of the vortex pairing noise near the wind tunnel lips.

5. Conclusion

Several 2D and 3D compressible DNS of a CD airfoil at a geometrical angle of attack of 8° and a Reynolds number based on the chord of 1.5×10^5 have been achieved with LBM as implemented in PowerFLOW. Both free-field and installed configurations in an open-jet anechoic wind tunnel mimicking measurements repeated in several different test facilities have been considered for the first time. All simulations evidence at least two main airfoil self-noise sources as found in previous DNS on NACA airfoils at lower Reynolds numbers: the LSB and the turbulent eddies near the trailing edge.

As previously shown with RANS simulations of the free-field and full test facility cases, neglecting the flow confinement induced by the jet on the airfoil (similar to a cascade solidity effect) alters the mean airfoil loading yielding a more intense and thicker LSB at the airfoil leading edge and different turbulent flow near the trailing edge. The far-field noise is consequently significantly altered with a much larger leading-edge contribution coming from the LSB. A different balance of airfoil self-noise sources is therefore observed. The 2D case including the nozzle jet recovers the mean airfoil loading and the location of the transition to turbulence triggered by the LSB re-attachment. Yet, the consequent development of the turbulent boundary layer is not proper as the turbulent eddies are not allowed to stretch in the spanwise direction, yielding too large coherent structures near the airfoil trailing edge and a too high low-frequency content in the wall-pressure fluctuations and a significant overestimate (more than 10 dB) of the far-field noise. This unambiguously shows that 2D DNS at a Reynolds number beyond 10^5 are unrealistic and may lead to improper estimates of the noise sources both in terms of relative amplitudes and frequency content.

The 3D simulation of the full wind-tunnel set-up on the other hand shows excellent agreement with the flow dynamics around the airfoil and the far-field acoustic pressure. Yet, the development of the jet shear layers is under resolved in the initial 3D DNS

(see Table 1) and does not match the hot-wire measurements at ECL. Two additional simulations, the 3D DNS-SLR and 3D DNS-SLRT, have then been conducted to better resolve the jet shear layer and its effect on the airfoil trailing-edge noise. The observed consequences are two-fold: on the one hand, the coupling between the jet and the airfoil is strong, yielding increased turbulence intensity upstream of the airfoil leading edge, variations in the LSB size, undulations of the effective angle of attack and variations in the wall-pressure fluctuations, the noise sources; on the other hand, the state of the jet shear layer at the nozzle exit of a given open-jet anechoic wind tunnel is found to influence the flow field around the airfoil and the consequent airfoil noise radiation with potentially a larger overlapping of jet noise over airfoil self-noise caused by vortex pairing in the jet shear layers. This strongly suggests not only to characterize the airfoil flow field and acoustics in airfoil-noise experiments, but also the jet state at the nozzle exit. The present effects are bound to be even stronger at higher angles of attack.

CRediT authorship contribution statement

Ziyang Zhou: Writing – review & editing, Writing – original draft, Visualization, Validation, Methodology, Investigation, Formal analysis, Conceptualization. **Stéphane Moreau:** Writing – review & editing, Supervision, Resources, Methodology, Funding acquisition, Conceptualization. **Marlène Sanjosé:** Writing – review & editing, Supervision, Resources, Methodology, Conceptualization.

Declaration of competing interest

The authors declare that they have no known competing financial interests or personal relationships that could have appeared to influence the work reported in this paper.

Acknowledgments

The authors acknowledge Calcul Quebec and Digital Research Alliance of Canada for providing the necessary computational resources for this research, and Dassault Systems for providing the Powerflow licenses and technical support. They also acknowledge the support of the Natural Sciences and Engineering Research Council of Canada (NSERC) through the Discovery grant.

Data availability

Data will be made available on request.

References

[1] R.E. Longhouse, Noise separation and design considerations for low tip-speed and axial-flow fans, J. Sound Vib. 48 (4) (1976) 461–474, http://dx.doi.org/10.1016/0022-460X(76)90550-2.
[2] F. Bellelli, R. Arina, F. Avallone, On the impact of operating condition and testing environment on the noise sources in an industrial engine cooling fan, Appl. Acoust. 227 (2025) 110252, http://dx.doi.org/10.1016/j.apacoust.2024.110252, 1–19.
[3] S. Oerlemans, P. Sijtsma, B.M. López, Location and quantification of noise sources on a wind turbine, J. Sound Vib. 299 (4–5) (2007) 869–883, http://dx.doi.org/10.1016/j.jsv.2006.07.032.
[4] B. Akhmetov, S. Gupta, K.K. Ahuja, Noise source ranking of a hairdryer, in: 20th AIAA/CEAS Aeroacoustics Conference, AIAA Paper 2014-3184, Atlanta, GA, 2014, http://dx.doi.org/10.2514/6.2014-3184.
[5] S. Moreau, Turbomachinery noise predictions: Present and future, Acoust. 1 (2019) 92–116, http://dx.doi.org/10.3390/acoustics1010008.
[6] S. Moreau, M. Roger, Competing broadband noise mechanisms in low-speed axial fans, AIAA J. 45 (1) (2007) 48–57, http://dx.doi.org/10.2514/1.14583.
[7] V. Pagès, P. Duquesne, S. Aubert, L. Blanc, P. Ferrand, X. Ottavy, C. Brandstetter, UHBR open-test-case fan ECL5/CATANA, Int. J. Turbomach. Propuls. Power 7 (2) (2022) 17, http://dx.doi.org/10.3390/ijtpp7020017.
[8] M. Wang, S. Moreau, G. Iaccarino, M. Roger, LES prediction of wall-pressure fluctuations and noise of a low-speed airfoil, Int. J. Aeroacoust. 8 (3) (2009) 177–197, http://dx.doi.org/10.1260/147547208786940017.
[9] H. Wu, S. Moreau, R.D. Sandberg, On the noise generated by a controlled-diffusion aerofoil at $Re_c = 1.5 \times 10^5$, J. Sound Vib. 487 (2020) 115620, http://dx.doi.org/10.1016/j.jsv.2020.115620, 1–25.
[10] M. Deuse, R.D. Sandberg, Different noise generation mechanisms of a controlled diffusion aerofoil and their dependence on Mach number, J. Sound Vib. 476 (2020) 115317, http://dx.doi.org/10.1016/j.jsv.2020.115317, 1–19.
[11] M. Sanjose, S. Moreau, Direct numerical simulation of self-noise of an installed control-diffusion airfoil, Can. Acoust. 39 (3) (2011) 30–31, URL: https://jcaa.caa-aca.ca/index.php/jcaa/article/view/2395 (Accessed 21 January 2025).
[12] M. Sanjose, C. Meon, S. Moreau, A. Idier, P. Laffay, Direct numerical simulation of acoustic reduction using serrated trailing-edge on an isolated airfoil, in: 20th AIAA/CEAS Aeroacoustics Conference, AIAA Paper 2014-2324, 2014, http://dx.doi.org/10.2514/6.2014-2324.
[13] M. Sanjosé, S. Moreau, B. Lyu, L.J. Ayton, Analytical, numerical and experimental investigation of trailing-edge noise reduction on a controlled diffusion airfoil with serrations, in: 25th AIAA/CEAS Aeroacoustics Conference, in: AIAA 2019-2450 Paper, Delft, The Netherlands, 2019, http://dx.doi.org/10.2514/6.2019-2450.
[14] M. Roger, S. Moreau, Broadband self noise from loaded fan blades, AIAA J. 42 (3) (2004) 536–544, http://dx.doi.org/10.2514/1.9108.
[15] S. Moreau, M. Roger, Effect of airfoil aerodynamic loading on trailing edge noise sources, AIAA J. 43 (1) (2005) 41–52, http://dx.doi.org/10.2514/1.5578.
[16] T. Padois, P. Laffay, A. Idier, S. Moreau, Detailed experimental investigation of the aeroacoustic field around a controlled-diffusion airfoil, in: 21st AIAA/CEAS Aeroacoustics Conference, in: AIAA 2015-2205 Paper, Dallas, TX, 2015, http://dx.doi.org/10.2514/6.2015-2205.
[17] P. Jaiswal, S. Moreau, F. Avallone, D. Ragni, S. Pröbsting, On the use of two-point velocity correlation in wall-pressure models for turbulent flow past a trailing edge under adverse pressure gradient, Phys. Fluids 32 (10) (2020) 105105, http://dx.doi.org/10.1063/5.0021121, 1–27.
[18] S. Lee, L. Ayton, F. Bertagnolio, S. Moreau, T.P. Chong, P. Joseph, Turbulent boundary layer trailing-edge noise: Theory, computation, experiment,and application, Prog. Aerosp. Sci. 126 (2021) 100737, http://dx.doi.org/10.1016/j.paerosci.2021.100737, 1–56.

[19] S. Moreau, M. Henner, G. Iaccarino, M. Wang, M. Roger, Analysis of flow conditions in freejet experiments for studying airfoil self-noise, AIAA J. 41 (10) (2003) 1895–1905, http://dx.doi.org/10.2514/2.1905.
[20] A.A. Sheikh-AlShabab, P.G. Tucker, Numerical investigation of installation effects in open jet wind tunnel airfoil experiments, in: 52nd Aerospace Sciences Meeting, in: AIAA 2014-1118 Paper, National Harbor, Maryland, 2014, http://dx.doi.org/10.2514/6.2014-1118.
[21] S. Moreau, M. Roger, J. Christophe, Flow features and self-noise of airfoils near stall or in stall, in: 15th AIAA/CEAS Aeroacoustics Conference (30th AIAA Aeroacoustics Conference), in: AIAA 2009-3198 Paper, Miami, Florida, 2009, http://dx.doi.org/10.2514/6.2009-3198.
[22] R.K. Amiet, Refraction of sound by a shear layer, J. Sound Vib. 58 (4) (1978) 467–482, http://dx.doi.org/10.1016/0022-460X(78)90353-X.
[23] A. McAlpine, B.J. Tester, Spectral broadening of tonal sound propagating through an axisymmetric turbulent shear layer, AIAA J. 58 (3) (2020) 1093–1106, http://dx.doi.org/10.2514/1.J058000.
[24] J. Jiao, Aeroacoustic Wind Tunnel Correction Based on Numerical Simulation (Ph.D. thesis), 2017, URL: https://elib.dlr.de/113499/.
[25] D.R. Neal, The Effects of Rotation on the Flow Field Over a Controlled-Diffusion Airfoil, Michigan State University, 2010, http://dx.doi.org/10.25335/vtj5-r172.
[26] J. Christophe, J. Anthoine, S. Moreau, Trailing edge noise of a controlled-diffusion airfoil at moderate and high angle of attack, in: 15th AIAA/CEAS Aeroacoustics Conference, in: AIAA 2009-3196 Paper, Miami, Florida, 2009, http://dx.doi.org/10.2514/6.2009-3196.
[27] J. Winkler, S. Moreau, T. Carolus, Large-eddy simulation and trailing-edge noise prediction of an airfoil with boundary-layer tripping, in: 15th AIAA/CEAS Aeroacoustics Conference, in: AIAA 2009-3197 Paper, Miami, Florida, 2009, http://dx.doi.org/10.2514/6.2009-3197.
[28] A. Arroyo Ramo, S. Moreau, R.D. Sandberg, M. Bauerheim, M.C. Jacob, Direct numerical simulation of controlled diffusion airfoil self-noise, in: 28th AIAA/CEAS Aeroacoustics 2022 Conference, in: AIAA 2022-2815 Paper, Southampton, UK, 2022, http://dx.doi.org/10.2514/6.2022-2815.
[29] C.K.W. Tam, H. Ju, Aerofoil tones at moderate Reynolds number, J. Fluid Mech. 690 (2012) 536–570, http://dx.doi.org/10.1017/jfm.2011.465.
[30] T.R. Ricciardi, W. Arias-Ramirez, W.R. Wolf, On secondary tones arising in trailing-edge noise at moderate Reynolds numbers, Eur. J. Mech / B Fluids 79 (2020) 54–66, http://dx.doi.org/10.1016/j.euromechflu.2019.08.015.
[31] Y. Kojima, C.S. Skene, C.-A. Yeh, K. Taira, M. Kameda, On the origin of quadrupole sound from a two-dimensional aerofoil trailing edge, J. Fluid Mech. 958 (2023) A3, http://dx.doi.org/10.1017/jfm.2023.37.
[32] H. Chen, Volumetric formulation of the lattice Boltzmann method for fluid dynamics: Basic concept, Phys. Rev. E 58 (3) (1998) 3955–3963, http://dx.doi.org/10.1103/PhysRevE.58.3955.
[33] H. Chen, S.A. Orszag, I. Staroselsky, S. Succi, Expanded analogy between Boltzmann kinetic theory of fluids and turbulence, J. Fluid Mech. 519 (2004) 301–314, http://dx.doi.org/10.1017/S0022112004001211.
[34] F. Avallone, W. Van Der Velden, D. Ragni, D. Casalino, Noise reduction mechanisms of sawtooth and combed-sawtooth trailing-edge serrations, J. Fluid Mech. 848 (2018) 560–591, http://dx.doi.org/10.1017/jfm.2018.377.
[35] M. Sanjose, A. Towne, P. Jaiswal, S. Moreau, S. Lele, A. Mann, Modal analysis of the laminar boundary layer instability and tonal noise of an airfoil at Reynolds number 150,000, Int. J. Aeroacoust. 18 (2–3) (2019) 317–350, http://dx.doi.org/10.1177/1475472X18812798.
[36] C. Teruna, F. Manegar, F. Avallone, D. Ragni, D. Casalino, T. Carolus, Noise reduction mechanisms of an open-cell metal-foam trailing edge, J. Fluid Mech. 898 (2020) A18, http://dx.doi.org/10.1017/jfm.2020.363.
[37] H. Chen, O. Filippova, J. Hoch, K. Molvig, R. Shock, C. Teixeira, R. Zhang, Grid refinement in lattice Boltzmann methods based on volumetric formulation, Phys. A 362 (1) (2006) 158–167, http://dx.doi.org/10.1016/j.physa.2005.09.036.
[38] P. Bradshaw, G.P. Huang, The law of the wall in turbulent flow, Proc. R. Soc. Lond. Ser. A 451 (1941) (1995) 165–188, http://dx.doi.org/10.1098/rspa.1995.0122.
[39] G. Bres, F. Pérot, D. Freed, Properties of the Lattice Boltzmann method for acoustics, in: 15th AIAA/CEAS Aeroacoustics Conference, in: AIAA 2009-3395 Paper, Miami, Florida, 2009, http://dx.doi.org/10.2514/6.2009-3395.
[40] Y. Li, R. Shock, R. Zhang, H. Chen, Numerical study of flow past an impulsively started cylinder by the Lattice-Boltzmann method, J. Fluid Mech. 519 (2004) 273–300, http://dx.doi.org/10.1017/S0022112004001272.
[41] T.F. Brooks, D.S. Pope, M.A. Marcolini, Airfoil Self-Noise and Prediction, NASA Reference Publication 19890016302, NASA Langley Research Center, 1989, http://dx.doi.org/10.2514/3.9426.
[42] J. Christophe, S. Moreau, C.W. Hamman, J.A.S. Witteveen, G. Iaccarino, Uncertainty quantification for the trailing-edge noise of a controlled-diffusion airfoil, AIAA J. 53 (1) (2015) 42–54, http://dx.doi.org/10.2514/1.J051696.
[43] J. Jeong, F. Hussain, On the identification of a vortex, J. Fluid Mech. 285 (1995) 69–94, http://dx.doi.org/10.1017/S0022112095000462.
[44] M. Breuer, Effect of inflow turbulence on an airfoil flow with laminar separation bubble: An LES study, Flow Turbul. Combust. 101 (2) (2018) 433–456, http://dx.doi.org/10.1007/s10494-017-9890-2.
[45] H. Wu, P. Laffay, A. Idier, P. Jaiswal, M. Sanjosé, S. Moreau, Numerical study of the installed controlled diffusion airfoil at transitional Reynolds number, in: Mathematical and Computational Approaches in Advancing Modern Science and Engineering, Springer, 2016, pp. 505–515, http://dx.doi.org/10.1007/978-3-319-30379-6_46.
[46] M.S. Istvan, J.W. Kurelek, S. Yarusevych, Turbulence intensity effects on laminar separation bubbles formed over an airfoil, AIAA J. 56 (4) (2018) 1335–1347, http://dx.doi.org/10.2514/1.J056453.
[47] T.P. Chong, P.F. Joseph, P. Davies, Design and performance of an open jet wind tunnel for aero-acoustic measurement, Appl. Acoust. 70 (4) (2009) 605–614, http://dx.doi.org/10.1016/j.apacoust.2008.06.011.
[48] P. Jaiswal, J. Rendón, S. Moreau, Aeroacoustic investigation of airfoil at near-stall conditions, Phys. Fluids 35 (9) (2023) http://dx.doi.org/10.1063/5.0166646.
[49] R. Sandberg, Compressible-flow DNS with application to airfoil noise, Flow Turbul. Combust. 95 (2015) 211–229, http://dx.doi.org/10.1007/s10494-015-9617-1.
[50] R.K. Amiet, Noise due to turbulent flow past a trailing edge, J. Sound Vib. 47 (3) (1976) 387–393, http://dx.doi.org/10.1016/0022-460X(76)90948-2.
[51] M. Roger, S. Moreau, Back-scattering correction and further extensions of Amiet's trailing-edge noise model. Part 1: theory, J. Sound Vib. 286 (3) (2005) 477–506, http://dx.doi.org/10.1016/j.jsv.2004.10.054.
[52] S. Moreau, P. Laffay, A. Idier, N. Atalla, Several noise control of the trailing-edge noise of a controlled-diffusion airfoil, in: 22nd AIAA/CEAS Aeroacoustics Conference, AIAA Paper 2016-2816, Lyon, France, 2016, http://dx.doi.org/10.2514/6.2016-2816.
[53] S. Moreau, M. Sanjosé, F. Perot, M.-S. Kim, Direct self-noise simulation of the installed controlled diffusion airfoil, in: 17th AIAA/CEAS Aeroacoustics Conference, AIAA Paper 2011-2716, Portland, Oregon, 2011, http://dx.doi.org/10.2514/6.2011-2716.
[54] C. Bogey, C. Bailly, Influence of nozzle-exit boundary-layer conditions on the flow and acoustic fields of initially laminar jets, J. Fluid Mech. 663 (2010) 507–538, http://dx.doi.org/10.1017/S0022112010003605.